Research Square

Preprints are preliminary reports that have not undergone peer review.
They should not be considered conclusive, used to inform clinical practice,
or referenced by the media as validated information.

Sustainable Utilization of Biomass-Derived Biochar for Asphalt Modification: Multiscale Experimental and Theoretical Insights

Meili Liu
University of Miami https://orcid.org/0009-0009-5324-2779
Shaocheng Shen
University of Miami
Kun Wang
University of Miami
Fuwu Zhang
University of Miami
Xianming Shi
xxs784@miami.edu

University of Miami

Research Article

Keywords: Biomass-derived carbon, Biochar, Waste valorization, Sustainable asphalt materials, Interfacial interactions, Density functional theory

Posted Date: May 13th, 2026

DOI: https://doi.org/10.21203/rs.3.rs-9684666/v1

License: This work is licensed under a Creative Commons Attribution 4.0 International License.
Read Full License

Additional Declarations: The authors declare no competing interests.

Abstract

Wheat straw-derived biochar (WS-biochar), a sustainable carbon material produced from agricultural residues, represents a promising pathway for the valorization of biomass waste toward low-carbon infrastructure systems. However, the molecular mechanisms governing its interaction with asphalt binders remain insufficiently understood, particularly at the micro- and nanoscale where structural, chemical, and morphological features play key roles. In this study, WS-biochar was incorporated into PG 70 – 10 asphalt at varying loadings (0–10 wt%), and a combined experimental and density functional theory (DFT) approach was employed to investigate its effects on asphalt structure and properties. Comprehensive spectroscopic and nanoscale characterization (SEM, BET, XRD, Raman, FTIR, NMR, and AFM fast force mapping) revealed that moderate biochar content (4–6 wt%) enhances local aromatic ordering, reduces structural defects, and produces a more uniform nanoscale surface morphology and mechanical response. DFT calculations further demonstrated that WS-biochar strongly interacts with asphalt molecules through hydrogen bonding, π-π stacking, van der Waals forces, and charge-transfer-assisted polarization, significantly modulating electronic structures and increasing molecular polarity. These findings provide mechanistic insights into the reinforcing effects of WS-biochar and a scientific basis for the sustainable design of biochar-enabled infrastructure materials with improved performance and reduced environmental footprint.

1. Introduction

Asphalt is a complex petroleum-derived organic material widely used as a binder in transportation infrastructure due to its viscoelastic behavior and mechanical stability. Globally, asphalt pavements constitute a critical component of transportation infrastructure, facilitating economic development and human mobility. However, despite its extensive application, asphalt faces intrinsic challenges during service, including thermal susceptibility, oxidative aging, moisture-induced damage, and mechanical degradation under repetitive loading[1–3]. These issues not only compromise pavement longevity but also increase maintenance costs and environmental burdens[4].

To address these limitations, various modifiers have been explored to improve the structural stability and long-term durability of asphalt binders[5, 6]. In recent years, biochar, a carbon-rich material produced from the pyrolysis of biomass, has emerged as a promising sustainable additive for infrastructure materials due to its porous structure, high surface area, and rich surface chemistry.[7, 8]. As a renewable and low-cost byproduct of agricultural residues, biochar aligns with increasing global demand for environmentally sustainable materials and offers opportunities to reduce carbon footprint of transportation infrastructure[9, 10].

Although research on biochar-modified asphalt is still comparatively early, recent studies have demonstrated its feasibility and performance benefits. For example, the incorporation of biochar into asphalt binders has been shown to modify rheological behavior and improve resistance to deformation at high temperatures, attributed to the porous skeletal structure of biochar that stiffens the binder[11].

Other experimental work using crop straw biochar reported changes in binder viscosity, softening point, penetration, and apparent rheological behavior, verifying biochar's interaction with asphalt at multiple scales[12]. Additional research has also applied biochar from cotton seed, camelia shells, and coffee grounds to modify asphalt, modifying thermal and mechanical response and potentially influencing low-temperature behavior and emission characteristics[9]. Similarly, biochar derived from industrial hemp stalks was shown to improve aging resistance, reduce temperature susceptibility, and increase the high-temperature performance grade of asphalt binders, thereby enhancing their deformation resistance under high-temperature conditions, although low-temperature performance may decline with higher biochar content[13].

Despite these promising observations, the underlying mechanisms governing interfacial interactions between biochar and asphalt matrices remain incompletely understood, particularly at the molecular and electronic levels. A systematic investigation integrating multiscale experimental characterization and computational modeling is therefore necessary to elucidate how biochar modifies the structural, chemical, and mechanical properties of asphalt.

In this study, wheat straw (WS)-derived biochar (WS-biochar) was incorporated into PG 70 − 10 asphalt at varying loadings, and a comprehensive characterization protocol, including scanning electron microscope (SEM), Brunauer-Emmet-Teller (BET), powder X-ray diffraction (XRD), Raman spectroscope, Fourier transform infrared (FTIR) spectra, NMR spectroscopic techniques, Atomic force microscopy (AFM), and Density Functional Theory (DFT) simulations under B3LYP/6-31G (d, p) level, was employed to uncover the interaction mechanisms. This work aims to link the physicochemical properties of biochar with changes in the structural and molecular organization of asphalt matrices, providing mechanistic insights for the design of sustainable biochar-enabled infrastructure materials.

2. Materials and methods

2.1 Sample preparation

The base asphalt binder used in this study had a performance grade of PG 70 − 10. Biochar was derived from wheat straw through pyrolysis at 850°C and is hereafter referred to as WS in this work. Subsequently, the WS biochar was subjected to the standard operating procedure (SOP) prior to blending with asphalt. A schematic illustration of the grinding procedure is provided in the Supporting Information (Fig. S1). Representative images of the ground WS-biochar are shown in Fig. S2. Asphalt binders incorporating different contents of WS-based biochar (0%, 2%, 4%, 6%, 8%, and 10% by weight of asphalt) are denoted as AWS0, AWS2, AWS4, AWS6, AWS8, and AWS10, respectively, where AWS0 represents the neat asphalt binder. To prepare the WS-modified asphalt samples, 100 g of the base asphalt was heated to 150°C and poured into a mixing container. The required amount of WS biochar corresponding to the target composition was then added and blended at 980 rpm for 30 min while maintaining the temperature at 150°C.

2.2 Characterization

Particle size distribution (PSD) and key physical-chemistry prosperities of the as-received WS biochar were evaluated as part of the International Biochar Initiative (IBI) Laboratory Tests for Certification Program (Control Laboratories, Watsonville, CA 95076, USA, www.biocharlab.com). The PSD is shown in Fig. S2a, and the summarized physicochemical properties are listed in Table S1. After the grinding by SOP, the PSD of WS-biochar was shown in Fig. S2 b. The crystal structure of WS-biochar after grinding, raw asphalt (AWS0) and modified asphalt samples were investigated by using powder X-ray diffraction (XRD) patterns which were obtained on PANalytical Empyrean XRD instrument. The finely powdered materials were irradiated with CuKα radiation (λ = 1.54 Å) produced at 40 mA current and 40 kV voltage. The XRD patterns were obtained in high angle region (2θ = 8–65°) using a scan step size of 0.01°. Fourier transform infrared (FTIR) spectra were obtained in the wavenumber range of 4000 – 700 cm^{-1} to identify the nature of surface functional groups. The surface morphology of the WS-biochar was investigated using JEOL JSM-7100F scanning electron microscope (SEM) at the Biomedical Nanotechnology Institute at the University of Miami (BIONIUM) under a beam voltage of 30 kV. The total surface area (based on the Brunauer-Emmet-Teller (BET) model) and the micro- and meso-pore volumes (determined from the t-plot and Barrett, Joyner and Halenda (BJH) method, respectively) were determined using the nitrogen gas sorption technique on a Micromeritics ASAP 2020 Accelerated Surface Area and Porosimetry Analyzer. Before analysis, WS-biochar sample was vacuum degassed for 12 h at a temperature of 120 °C. The adsorption and desorption of isotherms were established at relative pressure (p/p_o) intervals of 0.1-1. In addition, the surface elemental compositions and the bonding situations were determined using an ESCALAB 250Xi X-ray photoelectron spectroscopy (XPS) (Thermo Fisher Scientific, USA). Magnetic properties for WS-biochar were characterized using a Bruker electron paramagnetic resonance (EPR) spectrometer. The ^{1}H NMR (300 MHz, Chloroform-d) spectroscopic techniques are well established to measure the proportion of protons in specific molecular environments. Raman spectra were collected on a Thermo Scientific DXR2xi Raman microscope using 532 nm excitation. To avoid high fluorescence background samples were initially exposed for 1–2 minutes with the laser set to 2 mW and focused through a 10X objective. For data collection the power was lowered to 0.1 mW and focused through a 100X objective. 3 to 5 points on each sample were averaged, each point being the average of 250 0.05-second scans. Atomic force microscopy (AFM) tapping mode was employed to characterize the surface morphology of the asphalt binders, while AFM fast force-mapping (FFM) mode was used to probe their nanoscale mechanical properties. FFM is based on force-distance curves acquired through rapid force-deflection feedback at rates significantly higher than those of conventional force mapping. For each pixel, an individual force-distance curve was recorded and analyzed via Johnson-Kendall-Roberts (JKR) model[14, 15] to simultaneously extract topographical information and mechanical parameters, including adhesion force and Young's modulus. All AFM measurements were conducted using a Cypher S instrument under ambient conditions in air. An AC240TS-R3 probe with a nominal spring constant of 2 N/m was employed. For region-resolved statistical analysis, the asphalt surface was classified into four representative microstructural regions, including bee-shaped crest areas, bee-shaped valley areas, surrounding micro-regions, and outer smooth zones, following established AFM-based criteria for asphalt binders[16]. For each sample, five representative regions were selected and imaged using FFM, and the mechanical

parameters were statistically analyzed based on the nanometer scale pixel-resolved force–distance curves within each region to ensure reproducibility.

2.3 Computational details

To study the chemical properties of asphalt molecules and interactions between WS-biochar and Asphalt, the asphalt molecular models and WS-biochar with Asphalt were optimized under functional group of B3LYP with the basis sets of 6-31G (d, p)[17, 18] using the GAUSSIAN 16 software[19]. Vibrational frequency analyses were also performed at the same level of theory to confirm that the obtained structures are true minima with no imaginary frequencies. To address the inadequate description of dispersion interactions using functional methods, DFT-D3 (BJ)[20] dispersion correction was incorporated into the simulation. More accurate energies were further evaluated by the B3LYP functional with larger basis sets 6-311G(d, p)[21] and DFT-D3[22] dispersion correction for single-point energy calculations after geometry optimization. The adsorption energy (E_{ads}) was calculated between WS-biochar and asphalt molecules, as $E_{ads} = E_{complex} - E_{sub} - E_{WS}$, where $E_{complex}$, E_{sub} and E_{WS} represent the total energy of the Asphalt molecules with WS-biochar, Asphalt molecules, and WS-biochar molecule, respectively. The ESP-mapped vdW surfaces, ESP extrema[23, 24], frontier molecular orbital (FMO)[25], and IGMH (Independent Gradient Model based on Hirshfeld partition)[26],were rendered using the VMD 1.9.3 program[27] combined with Multiwfn 3.8 program[28].

3. Results and discussion

3.1. Physiochemical properties and crystalline structure of WS-biochar doped Asphalt

Asphalt binder is a highly complex and heterogeneous material composed of a broad distribution of hydrocarbons and their derivatives, including aliphatic and aromatic species. The introduction of external modifiers can significantly perturb its molecular environment and supramolecular organization, thereby altering the overall physicochemical behavior of the binder. To elucidate how WS-biochar interacts with asphalt and contributes to the modification mechanisms, a comprehensive multiscale characterization protocol was established. First, the intrinsic physicochemical properties of WS-biochar were systematically examined, including PSD, microstructural morphology, functional groups, surface chemistry, porosity, and magnetic behavior. Subsequently, structural and spectroscopic analyses were conducted on the WS-biochar-asphalt mixtures to capture changes in crystalline order, carbon hybridization, functional groups, and local molecular environments. Together, this characterization framework enables a coherent correlation between the inherent attributes of WS-biochar and the multiscale structural modifications induced within the asphalt matrix.

3.1.1 Characterization for WS-biochar

The PSD of WS-biochar incorporated into asphalt in this study spanned 2.72–704 μm (Fig. S2b). The corresponding SEM micrographs revealed a channel-like structure with precisely defined pores, whose wall thickness ranged from 1.526–2.649 μm (Fig. 1a)[29, 30]. Nitrogen adsorption-desorption analysis showed that WS-biochar possessed a specific surface area of 13.266 $m^2 \cdot g^{-1}$ and a total pore volume of 0.0184 $cm^3 \cdot g^{-1}$ (Fig. 1b and 1c). The crystalline structure of WS-biochar was examined by XRD (Fig. 1d). The broad diffraction peak around 2θ = 15–30° was characteristic of amorphous carbon [31, 32] with randomly oriented aromatic sheets, while minor sharp peaks indicate the presence of inorganic components such as quartz, calcite, and Mg/Ca oxides[33–36]. Electron paramagnetic resonance (EPR) spectroscopy was employed to probe the presence of paramagnetic species in WS-biochar (Fig. 1e). A pronounced single-line resonance was observed at a magnetic field of approximately 3435 G, corresponding to a *g* value of ~ 2.003, which is characteristic of carbon-centered organic radicals commonly reported in biochar and other pyrolyzed carbon materials[37–39]. The relatively broad linewidth and asymmetric first-derivative signal indicate the presence of delocalized unpaired π-electrons associated with structural defects and disordered aromatic domains within the amorphous carbon matrix, such as edge carbon atoms, dangling bonds, and oxygen-containing surface functionalities. These persistent radicals are typically generated during high-temperature pyrolysis and stabilized by conjugated aromatic structures in carbonaceous materials. FTIR analysis identified carboxy (1832–3631 cm^{-1} and 1698 cm^{-1}),aromatic (1578 cm^{-1}), C-O (1114 cm^{-1}), and O-H (1114 cm^{-1}) groups (Fig. 1f) [40–44], while XPS characterization confirmed a surface composition of 81.37% C1s and 14.98% O1s, with C1s contributions from COO (11.7%), C = O (14.1%), C-O (21.1%), and C-C/C = C/C-H (53.1%), as well as Si-C (21.9%)[45, 46], and O1s contributions from C = O (59.5%) and O-H/C-O-C (40.5%) (Fig. 1g, 1h and 1i)[42, 47–50]. The corresponding values on elemental compositions and C1s, O1s were tabulated in Tables S2-S3. The functional group and surface chemistry information obtained from FTIR and XPS informed the construction of WS-biochar models used in subsequent molecular simulations of its interaction with asphalt components, and the assumptions and structural details of the model are summarized in Table S4.

3.1.2 X-ray diffraction (XRD) analysis for WS-biochar-asphalt mixtures

To elucidate the structural evolution induced by WS-biochar incorporation, XRD was employed to probe changes in the carbonaceous framework of the modified asphalt systems (Fig. 2a). All samples exhibit a broad diffraction feature in the range of 2θ = 15–30°, corresponding to the C(002) reflection of disordered carbon, which is characteristic of amorphous or turbostratic aromatic structures. With increasing WS-biochar content, the full width at half maximum (FWHM)[51, 52] of the C(002) peak shows a non-monotonic trend (Fig. S3a and Table S5) [53]. Specifically, the FWHM decreases markedly from the neat asphalt to samples containing up to 4–6 wt% WS-biochar, indicating an enhancement in local aromatic stacking order and a reduction in structural disorder. This indicates that moderate WS-biochar loadings (4–6 wt%) facilitate enhanced local stacking of aromatic domains within the asphalt matrix, likely due to favorable interfacial interactions. Beyond 6 wt% WS-biochar, however, the FWHM increases

again, implying a deterioration of structural ordering. This trend is accompanied by a corresponding increase in the effective dislocation density[54–56], which reaches a minimum at approximately 4–6 wt% biochar loading and then rises sharply at higher dosages (Fig. S3b and Table S5). The increase in defect density at elevated biochar contents can be attributed to particle agglomeration and interfacial heterogeneity, which introduce localized strain and disrupt the continuity of aromatic domains. The concurrent evolution of FWHM and dislocation density indicates the existence of an optimal WS-biochar loading those balances structural ordering and defect formation. Among the compositions investigated, the sample containing 6 wt% WS-biochar exhibits the lowest defect density and near-minimum FWHM, suggesting an optimal degree of graphitic-like ordering within the disordered carbon framework. This composition was therefore identified as the optimal WS-biochar content from a structural perspective.

In addition to the broad C(002) peak, weak diffraction features associated with the original biochar (Fig. 1d) structure are still discernible in the modified asphalt, although their intensity is attenuated. This partial retention of biochar motifs indicates that the carbonaceous framework undergoes local structural reorganization rather than complete disruption upon incorporation. The evolution of these features with biochar content reflects the interplay between particle dispersion, interfacial interactions, and local ordering within the asphalt matrix.

Overall, the XRD results suggest that moderate WS-biochar loadings (4–6 wt%) enhance the local ordering of carbonaceous domains while minimizing defect formation, whereas higher loadings introduce structural disorder. Both the trends in the broad C(002) peak and the retained biochar features provide a coherent picture of how WS-biochar incorporation modifies the asphalt microstructure.

3.1.3 Raman Spectroscopy for WS-biochar-asphalt mixtures

Raman spectra of the unmodified asphalt and WS-biochar-modified asphalt samples were shown in Fig. 2b, which confirms the presence of D band (~ 1348–1360 cm^{-1} from vibrations of disordered sp^2 bonded defected carbon, activated by structural imperfections such as edge sites and heteroatom-containing functionalities) and G band (~ 1591–1593 cm^{-1} from in-plane stretching vibration of sp^2-bonded carbon atoms within aromatic structures)[57–59]. The presence of both D and G bands in all samples indicates that the carbonaceous framework of the asphalt is dominated by disordered aromatic domains. Upon incorporation of WS-biochar, the overall spectral features remain unchanged, suggesting that WS-biochar does not introduce new carbon phases but rather integrates into the existing aromatic network of the asphalt matrix. The structural evolution is therefore mainly reflected in changes in the relative intensities of the D and G bands. As shown in Fig. 2b, the I_D/I_G ratio of neat asphalt is 0.7223 and exhibits a subtle but non-monotonic dependence on WS-biochar content, decreasing from 0.7241 at 2 wt% to a minimum of 0.6993 at 6 wt%, followed by a slight increase at higher loadings. The decrease in I_D/I_G at moderate WS-biochar contents (4–6 wt%) indicates reduced defect density and enhanced local aromatic ordering, suggesting that appropriate biochar addition promotes a more organized arrangement of sp^2 carbon domains within the asphalt matrix. In contrast, the increase in I_D/I_G at ≥ 8 wt% implies increased structural disorder, likely arising from biochar agglomeration and interfacial

heterogeneity. Notably, this trend closely parallels the XRD results, particularly the evolution of the C(002) peak FWHM and dislocation density, with both techniques consistently identifying 4–6 wt% WS-biochar as the optimal range. Among all compositions, the 6 wt% WS-biochar sample exhibits the lowest I_D/I_G value, corroborating the XRD-derived conclusion of an optimal balance between aromatic ordering and defect formation.

3.1.4 Fourier transform infrared (FTIR) spectra for WS-biochar-asphalt mixtures

The chemical changes induced by WS-biochar incorporation (AWS0, AWS2, AWS4, AWS6, AWS8 and AWS10) were measured through FTIR spectroscopy (Fig. 2c). All samples exhibit similar spectral features, with no pronounced shifts in characteristic adsorption bands across the tested compositions[59]. The major peaks include C-H stretching vibrations of hydrocarbons at 3054 − 2725 cm^{-1}, a C = O stretching vibration at 1704 cm^{-1}, C = C and N-H stretching vibrations at ~ 1600 cm^{-1}, and sulfoxide (S = O) stretching vibrations at 1307 and 1026 cm^{-1}. The absence of new absorption bands and the preservation of peak positions indicate that WS-biochar addition does not significantly alter the functional groups or chemical bonding environment of the asphalt matrix[60–62]. This observation is further consistent with the Raman analysis, where the D and G band positions remain largely unchanged across all samples. Together, the FTIR and Raman results suggest that WS-biochar incorporation does not introduce new carbon phases, but mainly affects the asphalt structure through physical interactions and reorganization of existing aromatic domains.

3.1.5 Nuclear magnetic resonance (NMR) spectroscopy for WS-biochar-asphalt mixtures

The nuclear magnetic resonance (NMR) spectroscopy offers unique information on the chemistry of asphalt related materials[63]. Herein, in order to investigate the chemical interactions induced by WS-biochar incorporation, NMR spectroscopy was employed to probe potential changes in the hydrogen and carbon frameworks of the modified systems. Figure 2d show the ^1H NMR spectra of the asphalt samples containing different WS-biochar contents, respectively. Characteristic ^1H NMR spectra of the studied materials presented in Fig. 2d show intense peaks around 0.84–0.87 and 1.26–1.55 ppm which were attributed to methyl and methylene groups (aliphatic groups)[64].The peak centered at 7.28 ppm[65] and 0 ppm due to the deuterated chloroform ($CDCl_3$) and tetramethylsilane (TMS), respectively.

In raw asphalt (AWS0), the peak at ~ 5.30 ppm is assigned to vinylic protons (C = C-H), consistent with the Table of Characteristic Proton NMR Shifts[66]. Upon incorporation of WS-biochar, the 5.30 ppm signal progressively decreases in intensity and, in most formulations, disappears. This attenuation is consistent with paramagnetic broadening and signal quenching induced by unpaired electrons on the biochar surface. The EPR results (Fig. 1e), which confirm the presence of paramagnetic centers in WS-biochar, further support this interpretation. A new singlet at 2.17 ppm appears in the 8 wt% biochar sample (AWS8), likely corresponding to acetyl-type methyls ($-COCH_3$), suggesting a minor chemical

transformation or selective enrichment of this moiety upon biochar addition. To sum up, the ^{1}H NMR spectra of WS-biochar doped asphalt samples indicate that the chemical structure of asphalt binder was affected by the inclusion of WS-biochar.

3.2 Surface morphology and nanomechanical properties of WS-biochar doped Asphalt

3.2.1 Surface morphology and Roughness for WS-biochar-asphalt mixtures

Figure 3 showed the atomic force microscopy (AFM) surface microstructure of asphalt binder with different WS-biochar contents with the scan range of 10 μm, and the additional smaller scan range were shown in Fig. S4. The AFM topography (Fig. 3) revealed the characteristic bee-like microstructure in all samples, consisting of bright, elongated stiff domains embedded within a darker, softer continuous matrix. This morphology was widely associated with asphaltene-rich regions dispersed in a maltene- or wax-rich phase. The neat asphalt (AWS0) binder exhibited relatively small and uniformly distributed bee structures, representing a moderately phase-separated yet topographically smooth baseline. Upon biochar incorporation, the surface morphology evolves in a non-monotonic manner. At low biochar dosage (2 wt%, AWS2), the bee structures become enlarged and the height contrast between bright crests and dark valleys is amplified, indicating an initial disruption of the native microphase organization. In contrast, at intermediate biochar contents (4–6 wt%, AWS4 and AWS6), the bee-like structures become more finely distributed with a noticeable reduction in valley areas, suggesting a more homogenized microstructure. Such refinement and redistribution of bee-like domains are consistent with previous AFM-based studies[67] on biochar-modified asphalt, which reported that sludge-based biochar and waste wood-based biochar increases the number of bee-like structures while reducing their average area, thereby improving the uniformity of asphalt adhesion and enhancing overall interfacial bonding performance. At higher biochar contents (8–10 wt%, AWS8 and AWS10), increasingly elongated and partially coalesced bee domains are observed, indicative of renewed phase separation under over-saturated conditions.

To quantitatively assess whether these visually apparent morphological changes translate into measurable nanoscale topographic variations, the surface roughness was further analyzed. Although asphalt appears macroscopically smooth, AFM enables the resolution of nanoscale height fluctuations that are strongly influenced by microphase organization. The root mean square roughness (Rq) and arithmetic mean surface roughness (Ra), calculated from the AFM height data (Table 1), reflect the combined effects of the density, height variation, and spatial distribution of the bee-like domains. As shown in Table 1, Rq initially increases at low biochar content, consistent with the amplified bee-like topography observed at 2 wt%. At intermediate dosages (4–6 wt%), Rq decreases to values comparable to or slightly lower than that of the raw asphalt, indicating a smoother and more homogeneous nanoscale surface. At higher loadings (8–10 wt%), the roughness remains relatively moderate despite

the visually pronounced bee structures, suggesting that large-scale phase separation does not necessarily lead to increased nanoscale height fluctuations.

In addition to the dominant bee-like morphology, narrow line-shaped depressions are observed on the asphalt surface at biochar contents ≥ 4 wt%, with the highest prevalence at 6 wt% (Fig. 3). These features are characterized by shallow depths of approximately 1 nm, lateral extensions ranging from tens to hundreds of nanometers, and the absence of step-like height differences on either side, indicating that they arise from localized surface deformation rather than material removal. We attribute these linear depressions to subsurface imprints generated by plate-like or sharp-edged biochar fragments embedded near the shallow asphalt film. Due to the elastic-viscoelastic compliance of the thin asphalt overlayer, the presence of near-surface biochar platelets induces slight sagging or deformation along their edges, producing narrow grooves detectable by AFM. The pronounced appearance of these features at intermediate biochar contents suggests a dispersion threshold, where the probability of near-surface, surface-parallel biochar fragments is maximized. This interpretation is further supported by XRD analysis (Fig. 2a), which shows that the (002) diffraction peaks of the 4–6 wt% biochar composites become sharper and more intense, indicating enhanced stacking and preferred orientation of the biochar layers. When such oriented fragments reside approximately parallel to the asphalt surface, their subsurface presence more readily produces line-shaped shallow depressions in the overlying asphalt film, consistent with the AFM observations. Collectively, the AFM morphology, nanoscale roughness, and XRD results demonstrate that biochar content governs not only the degree of microphase separation but also the subsurface organization and surface compliance of asphalt binders, providing a mechanistic basis for the observed trends in adhesion and mechanical performance.

Table 1
Surface roughness of asphalt binder samples.

Sample	AWS0	AWS2	AWS4	AWS6	AWS8	AWS10
Rq (nm)	0.6544	5.8070	0.9161	1.3010	0.6662	1.4120
Ra (nm)	0.4228	3.4470	0.4870	0.7123	0.4246	0.6919

3.2.2 Nanomechanical heterogeneity revealed by FFM mapping

Fast force mapping (FFM) was further employed to resolve the nanoscale mechanical heterogeneity of WS-biochar-modified asphalt binders by simultaneously mapping surface topography, adhesion force, and Young's modulus (Fig. 4). The FFM topography exhibits trends consistent with the tapping-mode AFM observations (Fig. 3), confirming that the introduction of WS-biochar does not change the intrinsic type of surface microstructures in asphalt, but rather regulates their spatial distribution and statistical characteristics. The adhesion force[67] and Young's modulus maps (Fig. 4b and c) reveal pronounced mechanical contrasts that spatially coincide with the characteristic bee-like microstructure of asphalt. Importantly, the narrow line-shaped depressions (white arrow in Fig. S4) observed in tapping-mode AFM

are not discernible in either the adhesion or modulus maps. This indicates that these features do not represent mechanically distinct phases but instead arise from shallow geometric undulations of the asphalt surface, which are effectively averaged out under the applied FFM loading (~ 25 nN). The evolution of mechanical heterogeneity with biochar content further highlights the role of biochar dispersion. At low biochar content (2 wt%), the adhesion and modulus distributions become highly heterogeneous, indicating a strong perturbation of the native mechanical organization. In contrast, at intermediate biochar contents (4–6 wt%), the mechanical contrast between different regions is significantly reduced, suggesting a more uniformly reinforced and mechanically coherent near-surface structure. At higher loadings (8–10 wt%), the mechanical phase contrast becomes more pronounced again, reflecting the development of a highly differentiated phase assemblage under over-saturated conditions. Overall, the FFM results demonstrate that biochar content governs not only the morphological appearance but also the nanoscale mechanical heterogeneity of asphalt binders, providing independent mechanical evidence for the optimal dispersion window identified by AFM and XRD.

3.2.3 Statistical quantification of Nanomechanical properties

To quantitatively substantiate the mechanical trends inferred from the FFM maps, statistical analyses were conducted at both the global and spatially resolved levels (Fig. 5). The mean adhesion force and Young's modulus characterize the overall nanoscale mechanical response of the asphalt binders as a function of WS-biochar content (Fig. 5a and Table S6), whereas region-specific statistics across crest, valley, surrounding micro-regions, and smooth zones capture the evolution of mechanical heterogeneity and uniformity (Fig. 5b, c and Table S7). As shown in Fig. 5a and Table S8, the average adhesion force and Young's modulus exhibit a non-linear dependence on WS-biochar content. While low biochar loading (2 wt%) leads to increased dispersion of mechanical values, intermediate biochar contents (4–6 wt%) produce stabilized mean properties with reduced fluctuations. In contrast, further biochar addition (8–10 wt%) results in broadened distributions, reflecting the reintroduction of mechanical heterogeneity. These trends quantitatively mirror the non-monotonic evolution observed in the FFM maps. The spatially resolved statistics (Fig. 5b and c) further reveal that, although the relative ordering of mechanical properties among different surface regions (e.g., crest versus valley) is preserved across all samples, the magnitude of regional contrast is strongly biochar-dependent. In particular, the mechanical disparity between bee-like structures and smooth regions is minimized at intermediate biochar contents, indicating a suppression of localized mechanical extremes.

The coefficient of variation (CV) serves as a quantitative descriptor of nanoscale mechanical coherence. The CV (Fig. 5d-f and Table S6, Table S8) provides a direct metric of nanoscale mechanical uniformity. Both adhesion force and Young's modulus (Fig. 5d and e, f and Table S6, Table S8) exhibit minimum CV values at 4–6 wt% WS-biochar, signifying the highest degree of mechanical coherence across the asphalt surface. In contrast, elevated CV values at 2 wt% reflect dispersion-induced disorder, while the

increased CV observed at 8–10 wt% is consistent with aggregation-driven phase separation. These statistical signatures provide robust quantitative evidence that intermediate WS-biochar loadings yield an optimal balance between reinforcement and dispersion.

Taken together, the statistical analyses corroborate the spatially resolved FFM observations and confirm that WS-biochar induces a non-monotonic evolution of nanoscale mechanical heterogeneity in asphalt binders. An optimal dispersion window at intermediate biochar contents (4–6 wt%) produces a mechanically coherent near-surface structure, whereas under- and over-doped systems exhibit pronounced heterogeneity arising from disruption of native asphalt phases and biochar aggregation, respectively.

3.3 First-principles density functional theory (DFT) simulations

3.3.1 Electronic structure modulation of asphalt molecules induced by WS-biochar

In this work, the four-component twelve-molecule model proposed by Li and Greenfield[68, 69] was employed to represent the molecular-level physicochemical characteristics of asphalt binders. This model has been widely validated in reproducing key properties of asphalt systems and therefore provides a reliable basis for investigating biochar-asphalt interactions at the electronic scale. Electrostatic potential (ESP)[23, 24] analysis was first conducted to identify the intrinsic charge distribution and potential interaction sites of asphalt molecules (Fig. 6)[28]. As a representative example, the ESP distribution of benzobisbenzothiophene (Fig. 6a) exhibited distinct regions, with the color gradient from red to blue representing positive to negative potential. Local minima (cyan spheres) and maxima (yellow spheres) on the ESP surface indicate regions of electron density depletion and enrichment, respectively. The most negative ESP value (-14.98 kcal/mol) was located around the sulfur atom, identifying a pronounced electron-rich region favorable for electrophilic interactions and hydrogen-bond acceptance. Conversely, relatively positive ESP regions (19.83 kcal/mol) were located on hydrogen atoms associated with polar functional groups, highlighting potential sites for electrostatic attraction. The ESP distribution of WS-biochar (Fig. S5a) displays extensive electron-rich domains associated with heteroatom-containing functional groups and conjugated carbon structures. When WS-biochar is introduced into the asphalt system, substantial redistribution of the ESP is observed in the resulting complexes (Fig. S6), indicating pronounced electronic perturbation at the biochar-asphalt interface. The emergence of new extrema and the attenuation of original ESP contrasts collectively point to interfacial charge redistribution rather than simple geometric adsorption. The corresponding ESP values for all other asphalt molecules were summarized in Tables SS1-SS24 in TEXT II. These results demonstrate that ESP serves as the primary descriptor identifying where and why biochar preferentially interacts with specific asphalt molecular motifs, establishing the electrostatic foundation for adsorption and interfacial compatibility.

In addition, frontier molecular orbital (FMO) theory was applied to provides deeper insight into how WS-biochar alters the electronic structure and stability of asphalt molecules[25, 70, 71]. The highest occupied molecular orbitals (HOMOs) and the lowest unoccupied molecular orbitals (LUMOs) energies of the twelve asphalt molecules were analyzed (Fig. S7), together with those of WS-biochar (Fig. S5b, with the $\Delta E_{HOMO-LUMO}$ 1.2299 eV), to assess changes in electronic reactivity upon complex formation. Upon adsorption onto WS-biochar, the HOMO-LUMO gap (Fig. S8) of asphalt molecules decreases dramatically by approximately 52–96%, depending on molecular structure, with most systems exhibiting gap reductions in the range of 70–95% (Table S9). Such pronounced gap narrowing far exceeds the variations typically induced by conformational rearrangements and instead reflects strong electronic coupling and orbital hybridization between asphalt molecules and the biochar surface. From a physical perspective, the reduced HOMO-LUMO gap (Table S9) signifies facilitated electronic excitation and enhanced electronic polarizability of the complexes. More importantly, it indicates that WS-biochar induces a substantial reorganization of the electronic states of asphalt molecules, enabling charge-transfer-assisted noncovalent interactions, such as π-π stacking[72] and electrostatically stabilized adsorption. These findings provide direct electronic-structure evidence that the interaction between WS-biochar and asphalt is not merely dispersive but involves electron-level stabilization, consistent with the large adsorption energies and interfacial affinity observed in subsequent analyses.

To further quantify adsorption-induced electronic asymmetry, dipole moments were calculated as a complementary descriptor of molecular polarity[73]. In asphalt systems, molecular polarity is closely linked to intermolecular cohesion, aggregation behavior, and interfacial compatibility. Due to their intrinsically nonpolar nature, saturate molecules were excluded from this analysis. As summarized in Table S10, free asphalt molecules exhibit relatively low dipole moments, typically below 3 D, reflecting their weakly polar or quasi-nonpolar character. In sharp contrast, the formation of WS-biochar-asphalt complexes leads to a dramatic increase in dipole moment, with values rising to approximately 10–30 D, corresponding to an order-of-magnitude enhancement in molecular polarity. This substantial increase in dipole moment indicates strong adsorption-induced polarization driven by charge redistribution at the biochar-asphalt interface. The enhanced polarity reflects the development of asymmetric electron density and partial charge separation upon complex formation, which stabilizes the adsorbed state through long-range electrostatic interactions. Importantly, this polarization effect is fully consistent with the observed ESP redistribution and HOMO-LUMO gap narrowing, collectively demonstrating that WS-biochar acts as an electronic modulator that transforms weakly polar asphalt molecules into highly polarized interfacial complexes.

3.3.2 DFT-based analysis on between Asphalt and WS-biochar interactions

Figure 7a presented the adsorption energies of WS-biochar and WS-biochar-doped asphalt systems. The calculated adsorption energies (Table 2) indicated that all asphalt molecules interact favorably with WS-biochar, ranging from − 19.73 kcal/mol (e.g., DOCHN) to -46.89 kcal/mol (e.g., Pyrrole), confirming the

thermodynamic feasibility of adsorption. The optimized geometries (Fig. S9) revealed that asphalt molecules containing polar functional groups, such as hydroxyl, carbonyl, and heteroatoms, form close contacts or H-bond-like interactions with functional groups on the WS-biochar surface. Nonpolar regions primarily interact via van der Waals forces, indicating that adsorption is strongly influenced by molecular polarity and the spatial distribution of functional groups. For instance, the selected distances information in Pyrrole, PHPN, Hopane, Pyridinohopane and Quinolinohopane systems were highlighted in Figure S8, which correlates with its higher adsorption energy. To gain deeper insight into the specific types and spatial patterns of these weak interactions, IGMH (Independent Gradient Model based on Hirshfeld partition)[26] analysis was performed. Figure 7b showed the IGMH visualizations of interfragment weak interactions, highlighting hydrogen bonds (O/S···H, pink arrows), van der Waals contacts (brown arrows), and π-π stacking[72], C-H···π[74, 75], or O-H···π (σ-π) interactions (brown dashed arrows)[76], providing insights into the interaction patterns that govern the adsorption energies. These visualizations complement the adsorption energy and geometry analysis, providing a detailed picture of the interaction mechanisms governing adsorption in the WS-biochar-asphalt systems.

Table 2
Twelve representative asphalt molecules with their molecular formulas, molecular weights (Mr), and adsorption energies (E_{ad}) obtained from DFT calculations on WS-biochar.

Four-component	**Molecules**	**Molecular formula**	**Mr**	**E_{ad} (kcal/mol)**
Asphaltenes	Pyrrole	$C_{66}H_{81}N$	885.03	-46.89
	Phenol	$C_{42}H_{54}O$	582.55	-31.67
	Thiophene	$C_{51}H_{62}S$	722.71	-33.63
Naphthene Aromatics	PHPN	$C_{35}H_{44}$	452.44	-37.92
	DOCHN	$C_{30}H_{46}$	406.38	-19.73
Saturates	Hopane	$C_{35}H_{62}$	486.53	-26.60
	Squalane	$C_{30}H_{62}$	422.54	-25.36
Polar Aromatics (Resin)	Pyridinohopane	$C_{36}H_{57}N$	503.52	-26.89
	Quinolinohopane	$C_{40}H_{59}N$	561.60	-20.68
	Benzobisbenzothiopene	$C_{18}H_{10}S_2$	322.42	-20.26
	Trimethylbenzene-oxane	$C_{29}H_{50}O$	414.76	-32.76
	Thioisorenieratane	$C_{40}H_{60}S$	572.92	-31.46

4. Conclusions

This study introduced different percentages of WS-biochar into asphalt and systematically investigated the interactions between wheat straw biochar (WS-biochar) and asphalt at multiple scales using experimental characterization and DFT simulations. The main conclusions can be drawn as follows:

1. Structural and morphological effects: Moderate WS-biochar loadings (4–6 wt%) enhance local aromatic stacking, reduce structural defect density, and improve nanoscale surface uniformity, as evidenced by XRD, Raman, FTIR, NMR, and AFM analyses. Low (< 4 wt%) or high (> 6 wt%) loadings disrupt these features due to insufficient reinforcement or particle agglomeration.
2. Nanomechanical performance: Fast force mapping (FFM) reveals that intermediate biochar contents minimize mechanical heterogeneity, producing the most coherent adhesion and Young's modulus distribution. Low or excessive biochar contents lead to higher heterogeneity systems exhibit higher heterogeneity due to disrupted phase organization or aggregation.
3. Molecular-level interactions: DFT calculations show that WS-biochar interacts favorably with asphalt molecules via hydrogen bonding, π-π stacking, σ-π interactions (C-H···π, or O-H···π), van der Waals forces, and electrostatically stabilized interactions. These interactions induce electronic perturbations, reduce HOMO-LUMO gaps, and enhance molecular polarity, explaining the strong adsorption energies and improved interfacial compatibility.
4. Sustainability and application potential: WS-biochar incorporation not only enhances the mechanical and nanostructural properties of asphalt but also offers economic and environmental benefits, highlighting the potential of biochar as a sustainable carbon material for infrastructure applications.

Overall, this study provides a mechanistic framework connecting the physicochemical properties of WS-biochar with asphalt performance, guiding the rational design of biochar-enabled infrastructure materials.

Declarations

CRediT authorship contribution statement

Meili Liu: Writing-original draft, methodology, Formal analysis, Conceptualization, Visualization, Data curation, Software, Investigation. **Shaocheng Shen:** AFM data curation and analysis. **Kun Wang:** Writing-review & editing. **Fuwu Zhang:** Writing-review & editing. **Xianming Shi:** Conceptualization; Funding acquisition; Methodology; Project administration; Resources; Supervision; Writing-review and editing.

Acknowledgements

The authors would like to acknowledge the financial support by the United States Department of Agriculture (Grant No. 2025-68016-44163). All the simulations shown in this study were carried out using the supercomputer Triton, managed by the Institute of Data Science and Computing (IDSC) at the University of Miami. Shi. X is also thankful for the Early Career Researcher Award from the University of Miami's IDSC (Award No. EC202404). K.W. gratefully thanks for the support of the University of Miami Provost's Research Award (UM-PRA-2025-5714).

Data availability

Data will be made available on request.

References

1. Al-Qudsi A, Cannone Falchetto A, Wang D, Büchler S, Kim YS, Wistuba MP (2020) Finite element cohesive fracture modeling of asphalt mixture based on the semi-circular bending (SCB) test and self-affine fractal cracks at low temperatures. Cold Reg Sci Technol 169:102916. https://doi.org/10.1016/j.coldregions.2019.102916
2. Simms R, Hernando D, Roque R (2020) A new paradigm to explain the development of instability rutting in asphalt pavements. Road Mater Pavement Des 21:1815–1828. https://doi.org/10.1080/14680629.2019.1568286
3. Alae M, Zhao Y, Zarei S, Fu G, Cao D (2020) Effects of layer interface conditions on top-down fatigue cracking of asphalt pavements. Int J Pavement Eng 21:280–288. https://doi.org/10.1080/10298436.2018.1461870
4. Albuquerque FDB, Maraqa MA, Chowdhury R, Mauga T, Alzard M (2020) Greenhouse gas emissions associated with road transport projects: current status, benchmarking, and assessment tools. Transp Res Procedia 48:2018–2030. https://doi.org/10.1016/j.trpro.2020.08.261
5. Pei X, Fan W (2021) Influence of Compound Modification of Oil Sands De-Oiled Asphalt and Polyphosphoric Acid on High- and. Mater (Basel) 14:797. https://doi.org/10.3390/ma14040797. Low-Temperature Performance of Styrene-Butadiene-Styrene-Modified Asphalt
6. Yang Q, Lin J, Wang X, Wang D, Xie N, Shi X (2024) A review of polymer-modified asphalt binder: Modification mechanisms and mechanical properties. Clean Mater 12:100255. https://doi.org/10.1016/j.clema.2024.100255
7. Celauro C, Teresi R, Dintcheva NT (2023) Evaluation of Anti-Aging Effect in Biochar-Modified Bitumen. Sustainability 15:10583. https://doi.org/10.3390/su151310583
8. Saadeh S, Al-Zubi Y, Katawal P, Zaatarah B, Fini E (2023) Biochar effects on the performance of conventional and rubberized HMA. Road Mater Pavement Des 24:156–172. https://doi.org/10.1080/14680629.2021.2012238
9. Zhang X, Zhou Y, Xue Y (2025) Biochars from Cotton Seed, Camelia Seed Shell, and Coffee Ground in Modification of Asphalt: Fundamental Properties, Rheological Performance, and Inhibition of VOC Emissions. Mater (Basel) 18:1504. https://doi.org/10.3390/ma18071504
10. Dassanayake C, Mashaan NS (2025) Biochar as Additive and Modifier in Bitumen and Asphalt Mixtures. Eng 6:341. https://doi.org/10.3390/eng6120341
11. Ma F, Dai J, Fu Z, Li C, Wen Y, Jia M, Wang Y, Shi K (2022) Biochar for asphalt modification: A case of high-temperature properties improvement. Sci Total Environ 804:150194. https://doi.org/10.1016/j.scitotenv.2021.150194

12. Gan X, Zhang W (2021) Application of biochar from crop straw in asphalt modification. PLoS ONE 16:e0247390. https://doi.org/10.1371/journal.pone.0247390
13. Aslan İ, Tasdemir F, Tasdemir Y (2025) Utilization of biochar derived from industrial hemp stalks with various cooling methods for asphalt binder modification. PLoS ONE 20:e0325943. https://doi.org/10.1371/journal.pone.0325943
14. Ji X, Li J, Zhai X, Zou H, Chen B (2020) Application of Atomic Force Microscope to Investigate the Surface Micro-Adhesion Properties of Asphalt. Materials 13:1736. https://doi.org/10.3390/ma13071736
15. Johnson KL, Kendall K, Roberts AD (1971) Surface energy and the contact of elastic solids, Proc. A 324 301–313. https://doi.org/10.1098/rspa.1971.0141
16. Ma X, Wang D, Liu S, Jiang J, Kan J, Tu M (2024) Analysis of asphalt microscopic and force curves under water-temperature coupling with AFM. Case Stud Constr Mater 20:e03071. https://doi.org/10.1016/j.cscm.2024.e03071
17. Lee C, Yang W, Parr RG (1988) Development of the Colle-Salvetti correlation-energy formula into a functional of the electron density. Phys Rev B 37:785–789. https://doi.org/10.1103/PhysRevB.37.785
18. Becke AD (1993) Density-functional thermochemistry. III. The role of exact exchange. J Chem Phys 98:5648–5652. https://doi.org/10.1063/1.464913
19. Frisch MJ, Trucks GW, Schlegel HB et al (2016) Gaussian 16. Revision C. 01, https://gaussian.com/citation/
20. Grimme S, Ehrlich S, Goerigk L (2011) Effect of the damping function in dispersion corrected density functional theory. J Comput Chem 32:1456–1465. https://doi.org/10.1002/jcc.21759
21. Liu M, Huai Z, Tan H, Chen G (2021) Investigation of the Detailed AMPylated Reaction Mechanism for the Huntingtin Yeast-Interacting Protein E Enzyme HYPE. Int J Mol Sci 22:6999. https://doi.org/10.3390/ijms22136999
22. Grimme S, Antony J, Ehrlich S, Krieg H (2010) A consistent and accurate *ab initio* parametrization of density functional dispersion correction (DFT-D) for the 94 elements H-Pu. J Chem Phys 132:154104. https://doi.org/10.1063/1.3382344
23. Murray JS, Politzer P (2011) The electrostatic potential: an overview. WIREs Comput Mol Sci 1:153–163. https://doi.org/10.1002/wcms.19
24. Liu M, Tan H, Chen G (2020) Mechanistic insights of adenine promoted activity of low-molecule tyrosine phosphatase: An ONIOM study. Chem Phys Lett 754:137719. https://doi.org/10.1016/j.cplett.2020.137719
25. Yu J, Su NQ, Yang W (2022) Describing Chemical Reactivity with Frontier Molecular Orbitalets. JACS Au 2:1383–1394. https://doi.org/10.1021/jacsau.2c00085
26. Lu T, Chen Q (2022) Independent gradient model based on Hirshfeld partition: A new method for visual study of interactions in chemical systems. J Comput Chem 43:539–555. https://doi.org/10.1002/jcc.26812

27. Humphrey W, Dalke A, Schulten K, Molecular VMD-V, Dynamics (1996) J Molec Graphics 14:33–38
28. Lu T, Chen F (2012) Multiwfn: A multifunctional wavefunction analyzer. J Comput Chem 33:580–592. https://doi.org/10.1002/jcc.22885
29. Liang F, Liu Z, Jiang X, Li J, Xiao K, Xu W, Chen X, Liang J, Lin Z, Li M, Wu X, Wang H (2023) NaOH-modified biochar supported Fe/Mn bimetallic composites as efficient peroxymonosulfate activator for enhance tetracycline removal. Chem Eng J 454:139949. https://doi.org/10.1016/j.cej.2022.139949
30. Sahoo SS, Vijay VK, Chandra R, Kumar H (2021) Production and characterization of biochar produced from slow pyrolysis of pigeon pea stalk and bamboo. Clean Eng Technol 3:100101. https://doi.org/10.1016/j.clet.2021.100101
31. Huang Y, Yin X, Wu C, Wang C, Xie J, Zhou Z, Ma L, Li H (2009) Effects of metal catalysts on CO2 gasification reactivity of biomass char. Biotechnol Adv 27:568–572. https://doi.org/10.1016/j.biotechadv.2009.04.013
32. Mohan D, Abhishek K, Sarswat A, Patel M, Singh P, Pittman CU (2017) Biochar production and applications in soil fertility and carbon sequestration – a sustainable solution to crop-residue burning in India. RSC Adv 8:508–520. https://doi.org/10.1039/C7RA10353K
33. Singh B, Singh BP, Cowie AL (2010) Characterisation and evaluation of biochars for their application as a soil amendment. Soil Res 48:516–525. https://doi.org/10.1071/SR10058
34. Yang K-L, Ying T-Y, Yiacoumi S, Tsouris C, Vittoratos ES (2001) Electrosorption of Ions from Aqueous Solutions by Carbon Aerogel: An Electrical Double-Layer Model. Langmuir 17:1961–1969. https://doi.org/10.1021/la001527s
35. Liu Y, Zhao X, Li J, Ma D, Han R (2012) Characterization of bio-char from pyrolysis of wheat straw and its evaluation on methylene blue adsorption. Desalination Water Treat 46:115–123. https://doi.org/10.1080/19443994.2012.677408
36. Huang H, Reddy NG, Huang X, Chen P, Wang P, Zhang Y, Huang Y, Lin P, Garg A (2021) Effects of pyrolysis temperature, feedstock type and compaction on water retention of biochar amended soil. Sci Rep 11:7419. https://doi.org/10.1038/s41598-021-86701-5
37. Wang Y, Gu X, Huang Y, Ding Z, Chen Y, Hu X Insight into biomass feedstock on formation of biochar-bound environmentally persistent free radicals under different pyrolysis temperatures, RSC Adv 12 (n.d.) 19318–19326. https://doi.org/10.1039/d2ra03052g
38. Chen X, Alvarez PJJ, Masiello CA (2025) Environmentally Persistent Free Radicals in Biochar: Environmental Context and Future Research Needs. Environ Sci Technol 59:11440–11454. https://doi.org/10.1021/acs.est.4c13603
39. Guo C, Richmond-Bryant J (2021) Review of Environmentally Persistent Free Radical (EPFR) Solvent Extraction Methodology and Retrieval Efficiency. Chemosphere 284:131353. https://doi.org/10.1016/j.chemosphere.2021.131353
40. Mohan D, Singh P, Sarswat A, Steele PH, Pittman CU (2015) Lead sorptive removal using magnetic and nonmagnetic fast pyrolysis energy cane biochars. J Colloid Interface Sci 448:238–250.

https://doi.org/10.1016/j.jcis.2014.12.030

41. Cho D-W, Yoon K, Kwon EE, Biswas JK, Song H (2017) Fabrication of magnetic biochar as a treatment medium for As(V) via pyrolysis of FeCl3-pretreated spent coffee ground. Environ Pollut 229:942–949. https://doi.org/10.1016/j.envpol.2017.07.079
42. Sun Y, Yu IKM, Tsang DCW, Cao X, Lin D, Wang L, Graham NJD, Alessi DS, Komárek M, Ok YS, Feng Y, Li X-D (2019) Multifunctional iron-biochar composites for the removal of potentially toxic elements, inherent cations, and hetero-chloride from hydraulic fracturing wastewater. Environ Int 124:521–532. https://doi.org/10.1016/j.envint.2019.01.047
43. Niazi NK, Bibi I, Shahid M, Ok YS, Burton ED, Wang H, Shaheen SM, Rinklebe J, Lüttge A (2018) Arsenic removal by perilla leaf biochar in aqueous solutions and groundwater: An integrated spectroscopic and microscopic examination. Environ Pollut 232:31–41. https://doi.org/10.1016/j.envpol.2017.09.051
44. Oh S-Y, Seo Y-D, Ryu K-S (2016) Reductive removal of 2,4-dinitrotoluene and 2,4-dichlorophenol with zero-valent iron-included biochar. Bioresour Technol 216:1014–1021. https://doi.org/10.1016/j.biortech.2016.06.061
45. Zhao Q, Huang Y, Hu X (2016) A Si/C nanocomposite anode by ball milling for highly reversible sodium storage. Electrochem Commun 70:8–12. https://doi.org/10.1016/j.elecom.2016.06.012
46. Yu C, Zhang D, Dong X, Lin Q (2018) Pyrolytic behavior of a zero-valent iron biochar composite and its Cu(II) removal mechanism. RSC Adv 8:34151–34160. https://doi.org/10.1039/C8RA05676E
47. Lau AYT, Tsang DCW, Graham NJD, Ok YS, Yang X, Li X (2017) Surface-modified biochar in a bioretention system for *Escherichia coli* removal from stormwater. Chemosphere 169:89–98. https://doi.org/10.1016/j.chemosphere.2016.11.048
48. Ling L-L, Liu W-J, Zhang S, Jiang H (2017) Magnesium Oxide Embedded Nitrogen Self-Doped Biochar Composites: Fast and High-Efficiency Adsorption of Heavy Metals in an Aqueous Solution. Environ Sci Technol 51:10081–10089. https://doi.org/10.1021/acs.est.7b02382
49. Du H, Xi C, Tang B, Chen W, Deng W, Cao S, Jiang G (2022) Performance and mechanisms of NaOH and ball-milling co-modified biochar for enhanced the removal of Cd2 + in synthetic water: A combined experimental and DFT study. Arab J Chem 15:103817. https://doi.org/10.1016/j.arabjc.2022.103817
50. Chen L, Yang S, Zuo X, Huang Y, Cai T, Ding D (2018) Biochar modification significantly promotes the activity of Co3O4 towards heterogeneous activation of peroxymonosulfate. Chem Eng J 354:856–865. https://doi.org/10.1016/j.cej.2018.08.098
51. Shirokoff J, Lye L (2019) A Review of Asphalt Binders Characterized by X-ray Diffraction, Innovations in Corrosion and Materials Science (Formerly Recent Patents on Corrosion Science) 9. 28. https://doi.org/10.2174/2352094909666190401205036
52. Alshammari J, Alshammari J, Lewis JKC, Shirokoff J (2019) Nanosize Asphaltene in Asphalt Binders Characterized by X-ray Diffraction. Nanoparticle 1:1–4

53. Dehkhoda AM, Ellis N, Gyenge E (2014) Electrosorption on activated biochar: effect of thermo-chemical activation treatment on the electric double layer capacitance. J Appl Electrochem 44:141–157. https://doi.org/10.1007/s10800-013-0616-4
54. Das Bakshi S, Sinha D, Ghosh S, Chowdhury (2018) Anisotropic broadening of XRD peaks of α'-Fe: Williamson-Hall and Warren-Averbach analysis using full width at half maximum (FWHM) and integral breadth (IB). Mater Charact 142:144–153. https://doi.org/10.1016/j.matchar.2018.05.018
55. Nath D, Das R (2022) Assessing the dislocation density in CdSe nanocrystals from XRD peak profile analysis (XDPPA) assisted by first principles method. Physica E 144:115376. https://doi.org/10.1016/j.physe.2022.115376
56. Muiruri A, Maringa M, Preez Wdu (2020) Evaluation of Dislocation Densities in Various Microstructures of Additively Manufactured Ti6Al4V (Eli) by the Method of X-ray Diffraction. Materials 13:5355. https://doi.org/10.3390/ma13235355
57. Baludikay BK, François C, Sforna MC, Beghin J, Cornet Y, Storme J-Y, Fagel N, Fontaine F, Littke R, Baudet D, Delvaux D, Javaux EJ (2018) Raman microspectroscopy, bitumen reflectance and illite crystallinity scale: comparison of different geothermometry methods on fossiliferous Proterozoic sedimentary basins (DR Congo, Mauritania and Australia). Int J Coal Geol 191:80–94. https://doi.org/10.1016/j.coal.2018.03.007
58. Xu J, Liu J, Ling P, Zhang X, Xu K, He L, Wang Y, Su S, Hu S, Xiang J (2020) Raman spectroscopy of biochar from the pyrolysis of three typical Chinese biomasses: A novel method for rapidly evaluating the biochar property. Energy 202:117644. https://doi.org/10.1016/j.energy.2020.117644
59. Khairuddin FH, Md Yusof NI, Badri K, Ceylan H, Mohd Tawil SN (2019) Thermal, chemical and imaging analysis of Polyurethane / Cecabase modified bitumen, IOP Conf. Ser : Mater Sci Eng 512:012032. https://doi.org/10.1088/1757-899X/512/1/012032
60. Wei J, Li Y, Dong F, Feng H, Zhang Y (2014) Study on the amorphous poly alpha olefin (APAO) modified asphalt binders. Constr Build Mater 66:105–112. https://doi.org/10.1016/j.conbuildmat.2014.05.071
61. Omar HA, Md. Yusoff NI, Ceylan H, Rahman IA, Sajuri Z, Jakarni FM, Ismail A (2018) Determining the water damage resistance of nano-clay modified bitumens using the indirect tensile strength and surface free energy methods. Constr Build Mater 167:391–402. https://doi.org/10.1016/j.conbuildmat.2018.02.011
62. Al-Mansob RA, Ismail A, Rahmat RAOK, Borhan MN, Alsharef JMA, Albrka SI, Karim MR (2017) The performance of Epoxidised Natural Rubber modified asphalt using nano-alumina as additive. Constr Build Mater 155:680–687. https://doi.org/10.1016/j.conbuildmat.2017.08.106
63. Michon L, Martin D, Planche J-P, Hanquet B (1997) Estimation of average structural parameters of bitumens by 13C nuclear magnetic resonance spectroscopy. Fuel 76:9–15. https://doi.org/10.1016/S0016-2361(96)00184-6
64. Lambert JB, Mazzola EP, Ridge CD (2004) Nuclear Magnetic Resonance Spectroscopy. SENDON EDITION, WILEY, New Jersey

65. Nciri N, Kim J, Kim N, Cho N (2016) An In-Depth Investigation into the Physicochemical, Thermal, Microstructural, and Rheological Properties of Petroleum and Natural Asphalts. Materials 9:859. https://doi.org/10.3390/ma9100859
66. Table of Characteristic Proton NMR Shifts Table of Characteristic Proton NMR Shifts (n.d.). https://www.orgchemboulder.com/Spectroscopy/specttutor/nmrchart.shtml?
67. Li Q, Xu L, Chen X, Li W, Li Y, Wang H, Liu K (2024) Study on the Adhesion Performance of Biochar-Modified Asphalt Based on Surface Free Energy and Atomic Force Microscopy. Coatings 14:1390. https://doi.org/10.3390/coatings14111390
68. Xing C, Xiong Z, Lu T, Li H, Zhou W, Li C (2025) Performance of Asphalt Materials Based on Molecular Dynamics Simulation: A Review. Polymers 17:2051. https://doi.org/10.3390/polym17152051
69. Li DD, Greenfield ML (2014) Chemical compositions of improved model asphalt systems for molecular simulations. Fuel 115:347–356. https://doi.org/10.1016/j.fuel.2013.07.012
70. Parr RG, Yang W (1984) Density functional approach to the frontier-electron theory of chemical reactivity. J Am Chem Soc 106:4049–4050. https://doi.org/10.1021/ja00326a036
71. Fukui K, Yonezawa T, Shingu H (1952) A Molecular Orbital Theory of Reactivity in Aromatic Hydrocarbons. J Chem Phys 20:722–725. https://doi.org/10.1063/1.1700523
72. Saragi RT, Calabrese C, Juanes M, Pinacho R, Rubio JE, Pérez C (2023) Lesarri, π-Stacking Isomerism in Polycyclic Aromatic Hydrocarbons: The 2-Naphthalenethiol Dimer. J Phys Chem Lett 14:207–213. https://doi.org/10.1021/acs.jpclett.2c03299
73. Atkins P, de Paula J, Keeler J (2018) Atkins' Physical Chemistry, 11th edn. Oxford University Press, Oxford. https://chemistry.com.pk/books/atkins-physical-chemistry-11e/
74. Kar T, Bettinger HF, Scheiner S, Roy AK (2008) Noncovalent π – π Stacking and CH—π Interactions of Aromatics on the Surface of Single-Wall Carbon Nanotubes: An MP2 Study. J Phys Chem C 112:20070–20075. https://doi.org/10.1021/jp807809u
75. Kishida N, Tanaka Y, Yoshizawa M (2022) CH-π Multi-Interaction-Driven Recognition and Isolation of Planar Compounds in a Spheroidal Polyaromatic Cavity. Chemistry 28:e202202075. https://doi.org/10.1002/chem.202202075
76. Alonso M, Woller T, Martín-Martínez FJ, Contreras-García J, Geerlings P, De Proft F (2014) Understanding the Fundamental Role of π/π, σ/σ, and σ/π Dispersion Interactions in Shaping Carbon-Based Materials, Chemistry –. Eur J 20:4931–4941. https://doi.org/10.1002/chem.201400107

Figures

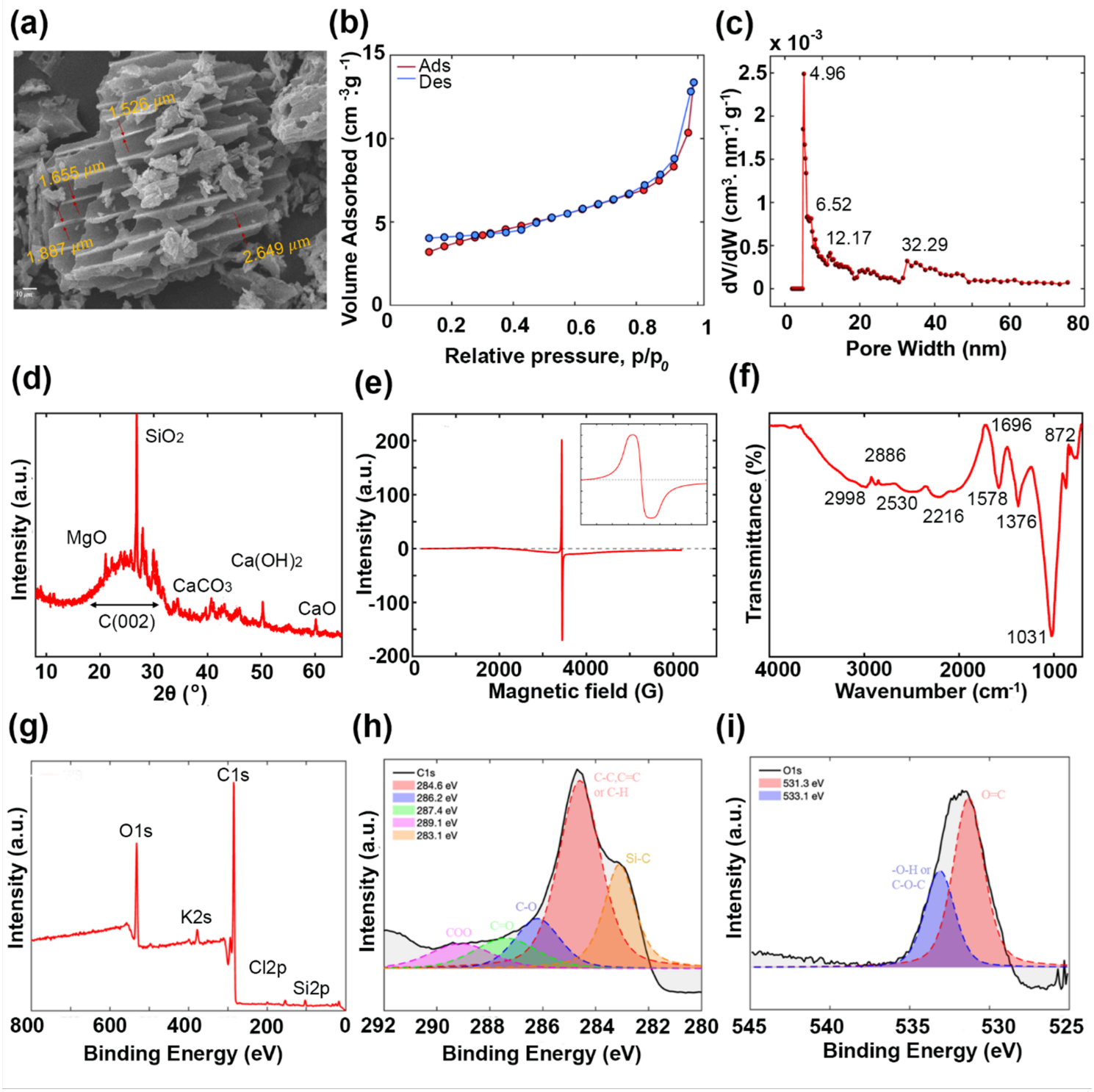


Figure 1

Comprehensive characterization of the biochar sample. (a) SEM image showing the surface morphology and microstructure of WS-biochar. (b) N_2 adsorption isotherms (BET) of WS-biochar (c) Corresponding pore size distribution derived from BET. (d) XRD patterns and (e) EPR signals were detected in WS-biochar. (f) FTIR spectra of WS-biochar, revealing its crystalline structure and functional groups. (g) XPS survey spectrum, indicating the elemental composition. (h) High-resolution XPS spectra

of C1s, showing the surface chemical states. (i) High-resolution XPS spectra of O1s, showing the surface chemical states.

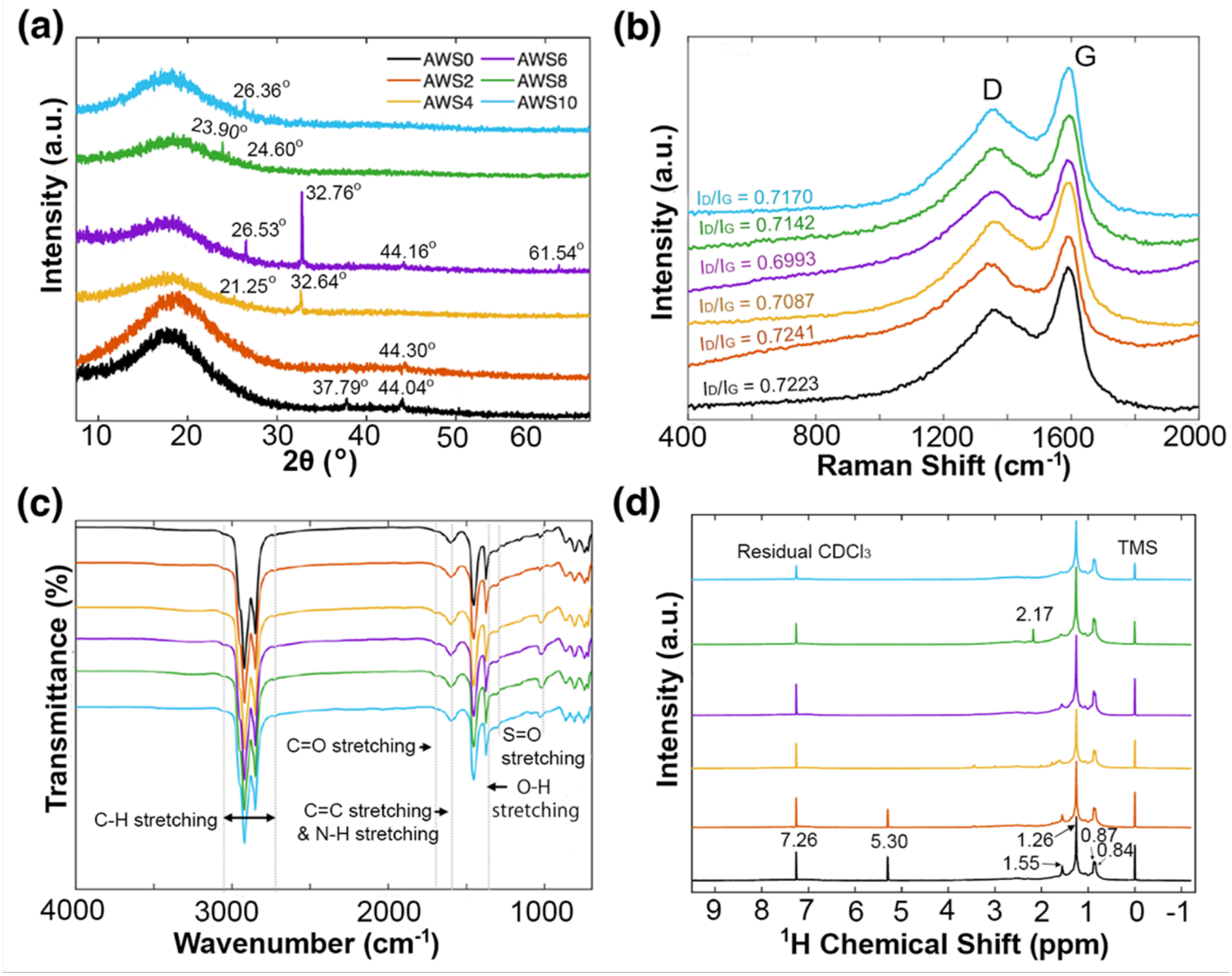


Figure 2

Physiochemical properties and crystalline structure characterization of asphalt samples with the different ratios (0, 2, 4, 6, 8, 10 wt%) of Asphalt to biochar. (a) X-ray diffraction patterns (XRD) patterns, (b) FTIR spectra, (c) Raman spectra, (d) ^{1}H NMR spectra. The color coding used to distinguish different biochar contents is indicated in panel (a) and is consistent across all panels.

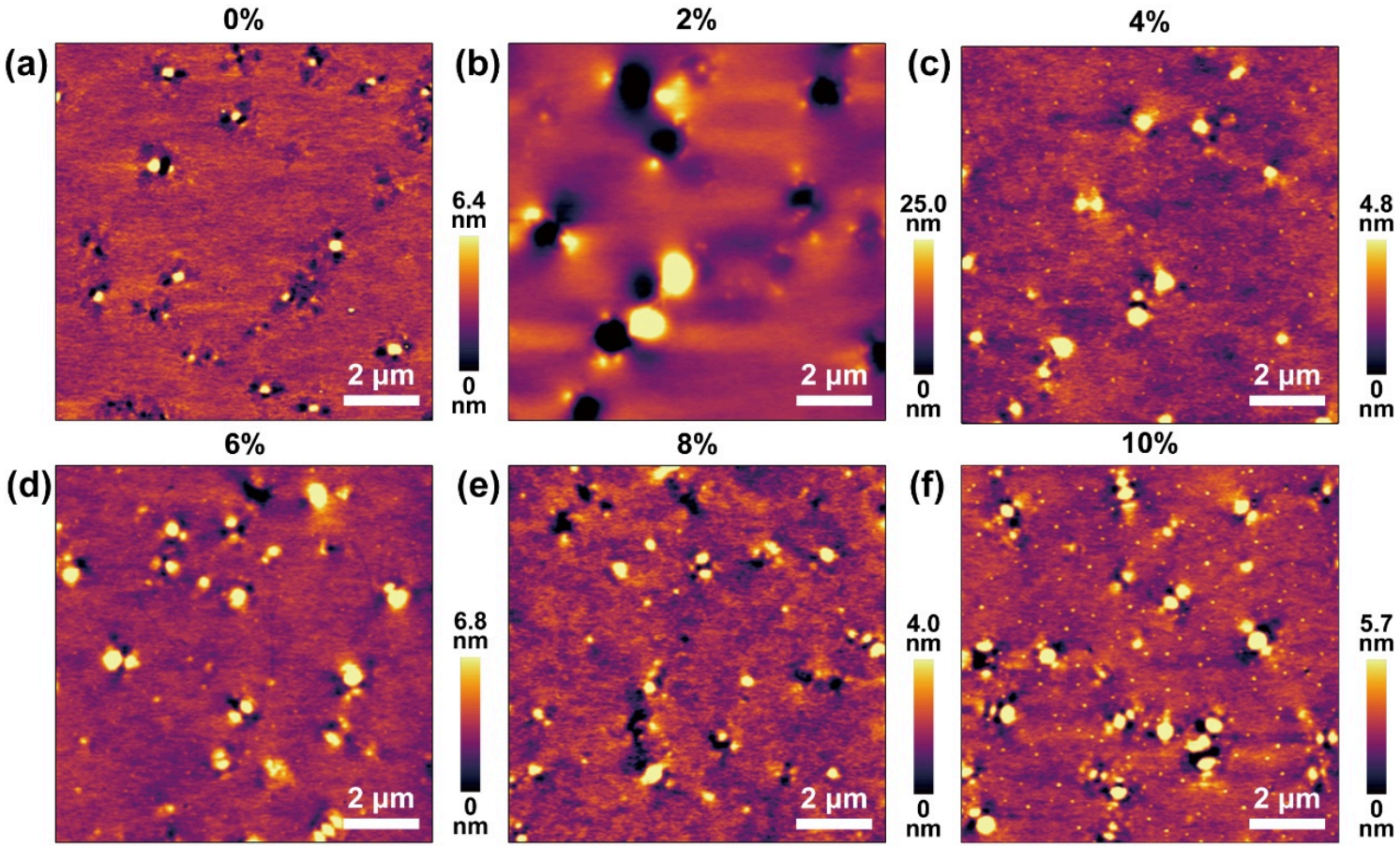


Figure 3

AFM images of the PG70-10 asphalt with biochar doping levels of (a) 0 wt%, (b) 2 wt%, (c) 4 wt%, (d) 6 wt%, (e) 8 wt% and (f) 10 wt%.

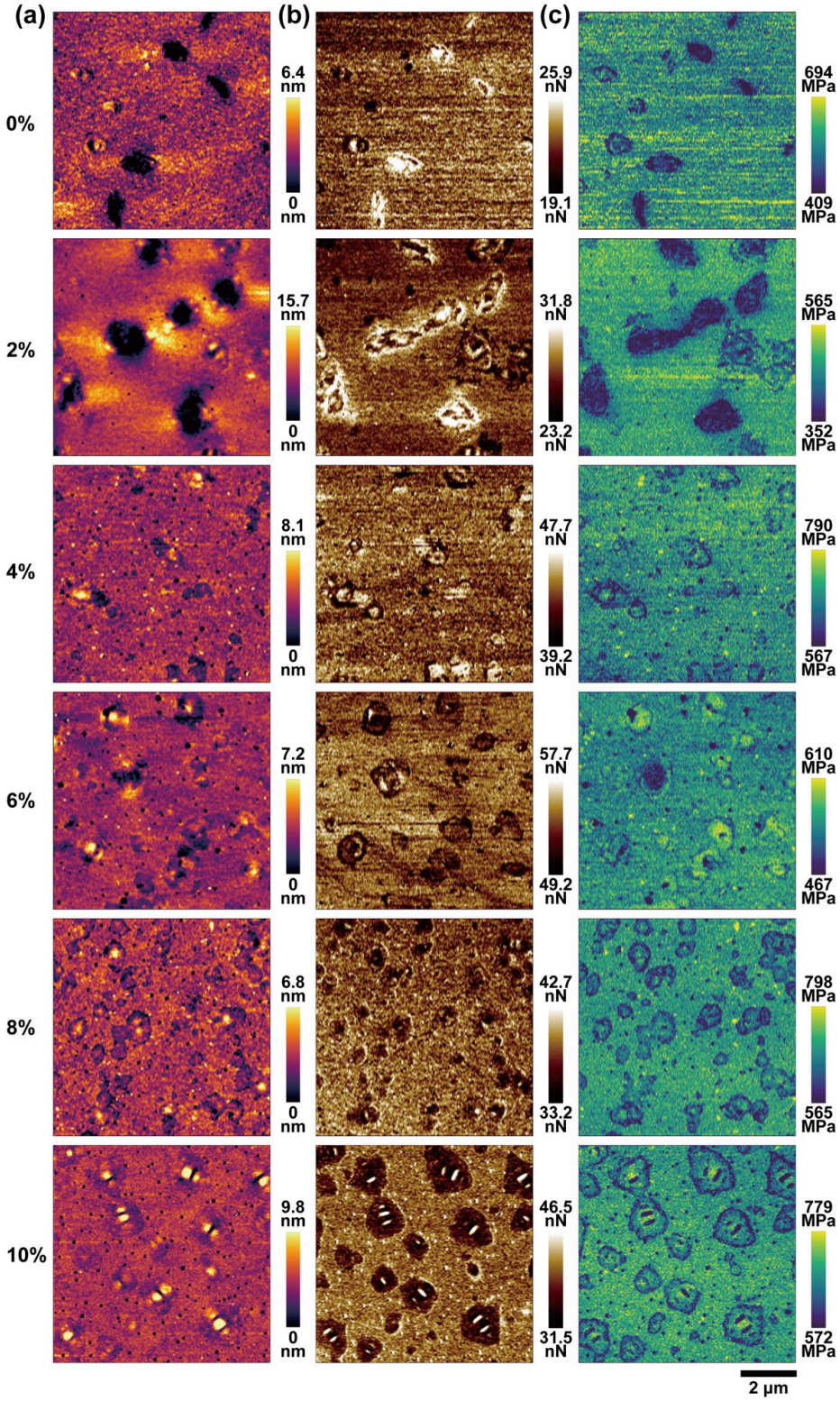


Figure 4

(a) AFM images of the PG70-10 asphalt with biochar doping levels of 0 wt%, 2 wt%, 4 wt%, 6 wt%, 8 wt%, and 10 wt%, acquired using fast force-mapping (FFM) mode. In this mode, each pixel corresponds to an individual force-distance curve collected during rapid force-spectroscopy scanning. The corresponding (b) adhesion force maps and (c) Young's modulus maps were obtained by extracting mechanical

parameters from the force-distance curve associated with each pixel. All images share the same scale bar.

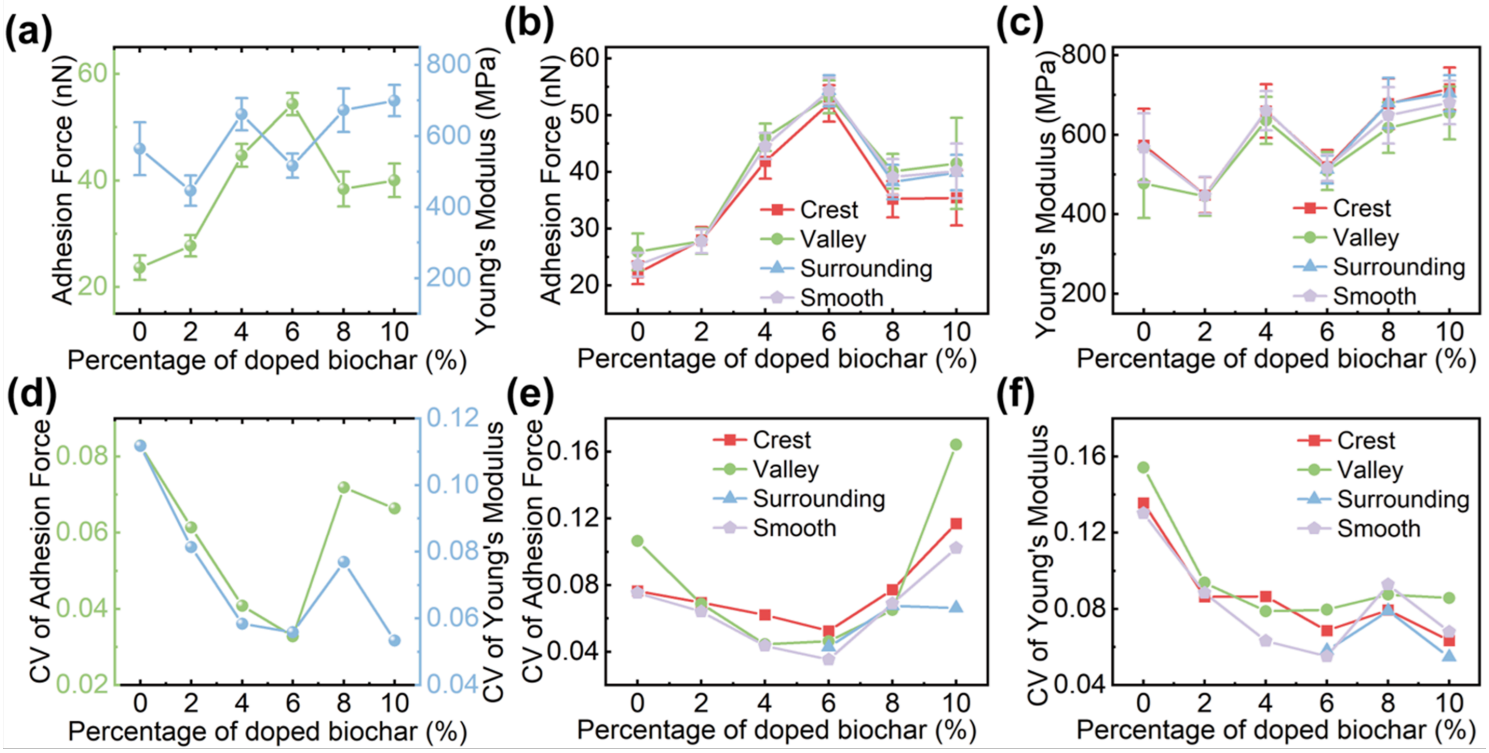


Figure 5

Mechanical properties of asphalt-biochar composites with varying asphalt-to-biochar ratios. (a) Adhesion force and Young's modulus of the asphalt binder samples, (b) Spatial distribution of Adhesion force across different surface regions of the asphalt binders (smooth zone, crest zone, valley zone, and surrounding zone). (c) Spatial distribution of Young's modulus across the same surface regions, (d) Coefficient of Variation (CV) of Adhesion Force and Young's Modulus, and (e) CV of Adhesion force distribution across different surface regions of the asphalt binders, (f) CV of Young's modulus distribution across different surface regions of the asphalt binders.

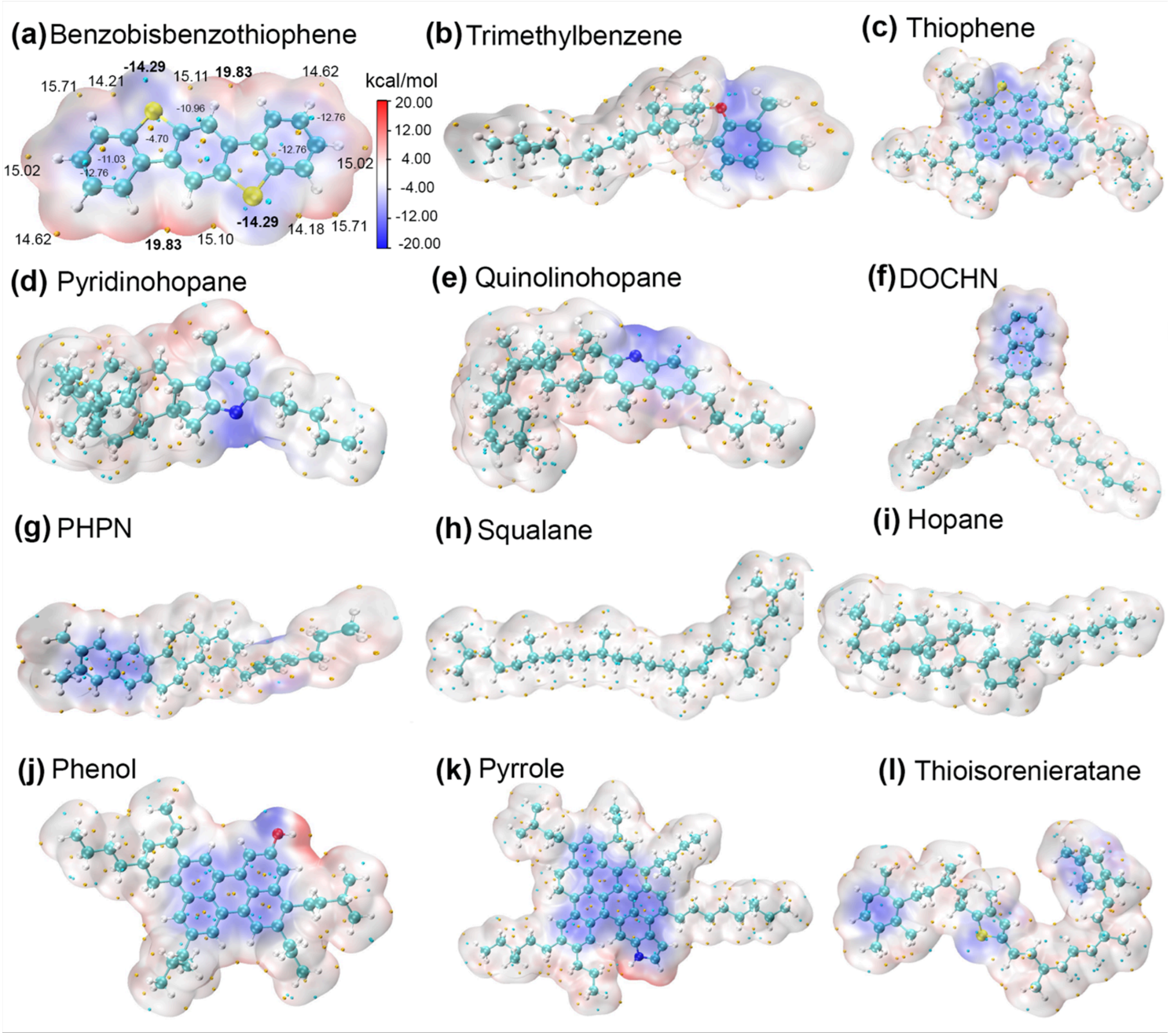


Figure 6

Electrostatic potentials (ESP) on the molecular vdW surface of 12 asphalt molecules with Resin (a, b, c, d and e), Naphthene Aromatics (f, g), Saturates (h, i), and Asphaltenes (j and k). All the ESP calculations are performed at the level of B3LYP/6-31G (d, p). Yellow and cyan spheres denote the surface local maxima and minima of the ESP values.

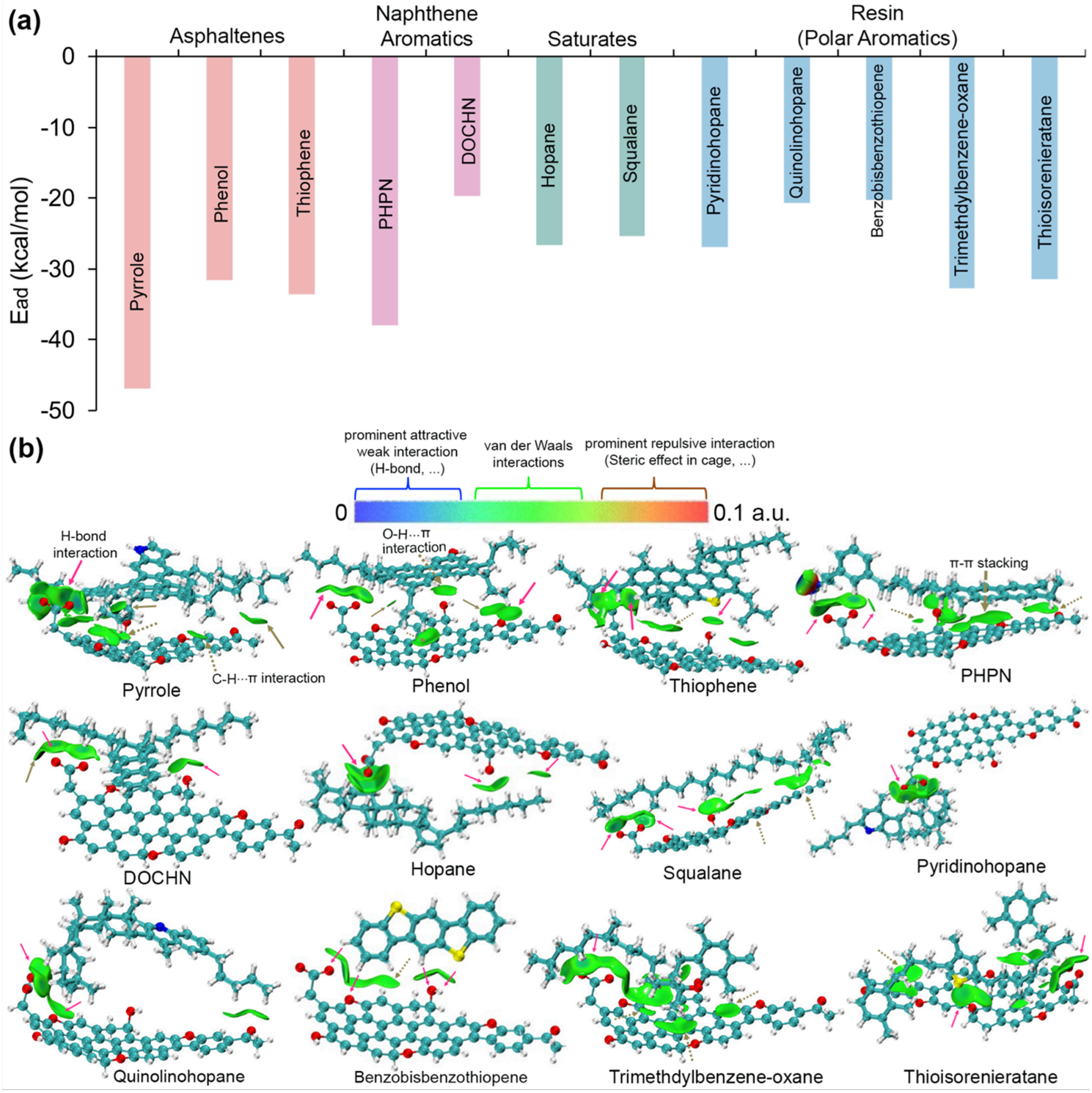


Figure 7

Adsorption energies (a) and optimized geometries (b) of WS-biochar-doped asphalt systems. All distances are reported in angstroms (Å).

Supplementary Files

This is a list of supplementary files associated with this preprint. Click to download.

- TEXTISupportingInformation.docx
- TEXTIISupportingInformation.docx
- GA.jpeg